J Mater Sci (2017) 52:5309–5323

Understanding the structure–property relationships of the ferroelectric to relaxor transition of the $(1 - x)BaTiO_3$–$(x)BiInO_3$ lead-free piezoelectric system

Alicia Manjón-Sanz[1], Caitlin Berger[1], and Michelle R. Dolgos[1,*]

[1] *Department of Chemistry, Oregon State University, Corvallis, OR 97331, USA*

Received: 13 December 2016
Accepted: 7 January 2017
Published online: 25 January 2017

ABSTRACT

A structural and electromechanical investigation has been performed on $(1 - x)BaTiO_3$–$(x)BiInO_3$ in the region $0.03 \leq x \leq 0.12$. A gradual structural phase transition has been observed where the structure changes from tetragonal ($P4mm$) and passes through two regions of coexisting phases: (1) $P4mm + R3m$ in the range $0.03 \leq x \leq 0.075$ and (2) $Pm\bar{3}m + R3m$ for $0.10 \leq x \leq 0.12$. The properties also transition from ferroelectric ($x \leq 0.03$) to relaxor ferroelectric ($x \geq 0.05$) as the dielectric permittivity maximum becomes temperature and frequency dependent. This transition was also confirmed via polarization-electric field measurements as well as strain-electric field measurements. At the critical composition of $x = 0.065$, a moderate strain of $\sim$0.104% and an effective piezoelectric coefficient (d^*_{33}) of 260 pm/V were observed. The original purpose of this study was to demonstrate the polarization extension mechanism as predicted in the literature, but due to the ferroelectric to relaxor transition, this mechanism was not found to be present in this system. However, this demonstrates that $BaTiO_3$-based lead-free ceramics could be modified to obtain enhanced electromechanical properties for actuator applications.

Introduction

For the past two decades, there has been tremendous effort put into the search for lead-free piezoelectric materials to replace the industry standard $Pb(Zr_{1-x}Ti_x)O_3$ (PZT) [1, 2]. PZT remains the material of choice because it shows outstanding properties such as a high piezoelectric response ($d_{33} \sim$ 200–600 pC/N) [3], a good electromechanical coupling factor ($k_p \sim 0.67$), and can be easily modified by doping for tailored use in a large number of applications. However, PZT has several major performance disadvantages. It cannot operate above $\sim$150 °C, which severely restricts its use in high-temperature applications, and it suffers from stability issues due to

Address correspondence to E-mail: michelle.dolgos@oregonstate.edu

DOI 10.1007/s10853-017-0770-x

fatigue. Lead is not currently regulated in electronic devices, but the latest restriction of hazardous substance (RoHS) directive has extended this exemption only three years rather than the usual five years [4]. This change demonstrates that the need for new piezoelectric materials clearly exists, but there is currently no substitute for PZT.

Efforts to find new lead-free materials typically aim to mimic the morphotropic phase boundary (MPB) of PZT, which shows an enhanced piezoelectric effect. PZT's MPB can be derived from a polarization rotation mechanism which results in what can be called a classical MPB, one that lies between two ferroelectric phases with polar crystal structures [5–9]. However, another type of mechanism, called a polarization extension/contraction, exists as described by Damjanovic [8, 10]. A polarization extension occurs between a non-polar phase with a polarization vector of zero, and a polar phase with a non-zero value for the polarization vector. This mechanism can also create an MPB with an enhanced piezoelectric response like that found in a polarization rotation. Calculations have shown that like polarization rotation, a polarization extension occurs when the free energy profile at the boundary between the two phases flattens, allowing the phase to change with ease [10, 11]. The theoretical papers by Damjanovic have hypothesized that materials with a polarization rotation on one end of the MPB and a polarization extension on the other end of the MPB could potentially be very highly performing piezoelectrics. However, these systems have been largely ignored in the literature. A few of the known systems that report a polarization extension include $BaTiO_3$–$BaSnO_3$ [11], AlN–ScN [12, 13], and KH_2PO_4 [14]. It has been predicted that $BaTiO_3$–$BiInO_3$ synthesized by Datta et al. has an MPB derived from a polarization extension mechanism, but the properties had not been measured [10, 15].

$BaTiO_3$ (BT) is a classical ferroelectric material and crystallizes in the non-centrosymmetric tetragonal space group $P4mm$ where the Ti atom is displaced from the center of the octahedra along [001] [16]. BT has a Curie temperature (T_c) of 120 °C where the polarization gives way to the cubic $Pm\bar{3}m$ structure and has a piezoelectric response (d_{33}) of 190 pC/N [17]. As with most pure Bi-based perovskites, $BiInO_3$ (BI) can only be synthesized at high pressure as it has a small tolerance factor (0.88) [18]. However, using BI in solid solutions with perovskites that have a higher tolerance factor like $PbTiO_3$ (PT) (1.019) [19, 20] or BT (1.06) [15] stabilizes this phase at ambient pressures. BI crystallizes in the non-centrosymmetric orthorhombic space group $Pna2_1$, and it decomposes into two phases upon heating above 600 °C with no structural phase transition recorded, indicating it remains ferroelectric at high temperatures until decomposition [18]. The electromechanical properties of BI have not been reported, but theoretical studies investigating its electronic properties using first principles consider it a promising dielectric material [21] and suggest that it is an excellent candidate for replacing the widely used ferroelectric and piezoelectric PT [22].

The solid solution $(1-x)$BT–(x)BI is thought to have a compositionally driven polarization extension mechanism as the structure changes from $P4mm$ ($x \leq 0.07$) → $P4mm + R3m$ ($x \sim 0.10$) → $Pm\bar{3}m$ ($0.10 < x < 0.25$) as the amount of BI increases [10, 15]. This structural change represents a possible MPB in the two phase region with a polarization rotation mechanism on the high BT side and a polarization extension mechanism on the low BT side. In this study, we have investigated the structure and electromechanical properties of the lead-free $(1-x)$BT–(x)BI system to determine whether this prediction is correct.

Experimental

Synthesis

Powder samples of $(1-x)$BT–(x)BI solid solutions were synthesized in the region $0.03 \leq x \leq 0.12$ following a standard solid-state synthesis route. $BaCO_3$ (Strem Chemicals Inc., 99.9%), TiO_2 (Alfa Aesar, 99.9%), Bi_2O_3 (Strem Chemicals Inc., 99.999%) and In_2O_3 (Alfa Aesar, 99.9%) were weighed in stoichiometric ratios where $BaCO_3$ was placed in a drying oven at 120 °C overnight prior to being weighed. The starting materials were ball milled in a planetary micromill (Pullverisette 7 Classic Line, Fritsch) for 24 h to obtain a homogeneous mixture. During ball milling, each sample was placed in a container with 25 ml of ethanol and eight 10 mm yttria-stabilized zirconia balls, for 45 cycles with each cycle consisting of 15 min forward, 10 min rest, and then 15 min reverse milling direction at a rate of 350 rpm. The resulting powders were calcined in alumina crucibles

at 1000 °C for 8 h. Next, 13-mm pellets were pressed and placed in closed crucibles and sintered at 1200 °C for 5 h buried in sacrificial powder of the same composition to prevent volatilization of bismuth oxide. The cooling and heating rate used was 3 °C/min. Several samples were sent to Galbraith Laboratories Inc for compositional analysis using ICP.

Pellet processing

For physical properties measurements, pellets with a density ≥95% of the crystallographic value were used as measured by an Archimedes balance. To obtain this high density, after the calcination step, the powders were thoroughly ground in a mortar and pestle and mixed with a 3 wt% polyvinyl butyral (Sigma Aldrich) binder. Then, 13-mm pellets were pressed in a uniaxial press, placed in latex bags and pressed at 210 MPa for 2 min using a cold isostatic press. The sintering conditions were the same as for sample preparation, with the exception of a binder burnout step added at 450 °C for 4 h prior sintering the pellets at 1200 °C for 5–15 h buried in sacrificial powder. Prior to measurement, all pellets were checked by X-ray diffraction (XRD) to ensure that no impurity phases were present.

Physical properties measurements

For polarization-electric field (*P*–*E*) and strain-electric field (*S*–*E*) measurements, pellets were polished down into to ≤0.3 mm thickness with a mirror finish using a semi-automatic polishing machine (LaboPol-5, Struers) with a series of P400, P1200, then P4000 SiC foils (Struers). For electrical contacts, silver conductive paint (SPI supplies #05002-AB) was applied on both sides of the pellets and any deposits on the edges were removed to avoid shorting. *P*–*E* and *S*–*E* experiments were performed with the pellet submerged in silicon oil at room temperature with frequency of 0.1 Hz using a Radiant high voltage test fixture sample holder attached to a standard ferroelectric test system (Radiant technologies). Measurements of strain as a function of electric field were carried out using an optical displacement sensor (MTI-2100).

High-temperature dielectric permittivity measurements were performed on pellets with thickness ranging from 0.5 to 1 mm. For electrical contacts, high-temperature silver conductive paste (Heraeus C1000) was applied to the pellets and cured at 750 °C for 2 h. The disks were then placed in a high-temperature measurement cell (NorECS Probostat) and inserted into a tube furnace equipped with a Eurotherm temperature controller. Capacitance and loss were collected against frequency and temperature by using an HP 4192A LF Impedance Analyzer and a LABVIEW program. Measurements were taken over the frequency range of 100 Hz–1 MHz over a temperature range from 25 to 230 °C. The heating and cooling rate used was 2 °C/min.

Diffraction experiments

XRD data were collected using a Rigaku Miniflex 600 diffractometer with Cu Kα radiation ($\lambda = 1.54056$ Å) to determine phase purity of the synthesized samples. Data were measured over a 2θ range from 5° to 60°.

Synchrotron X-ray diffraction (SXRD) data were collected on the beamline 11-BM at the Advanced Photon Source at Argonne National Laboratory [23]. Crushed powders of each composition were diluted with quartz wool to reduce adsorption and were loaded into Kapton capillaries which were spun during the measurement to achieve improved averaging of the powder. SXRD patterns were recorded at room temperature with a wavelength of 0.414219 Å, over 1 h, using standard data collection protocol (30 keV, multi-detector range covering approximately a 2θ range from 0.5° to 52°).

Neutron powder diffraction (NPD) data were collected on the POWGEN diffractometer at Oak Ridge National Laboratory. Approximately 3 g of each powder was loaded into a vanadium can, and NPD data were collected with a central wavelength of 1.066 Å covering a *d*-spacing of 0.276–4.606 Å at room temperature for approximately 2 h.

Combined Rietveld refinements utilizing both the SXRD and NPD data were performed using the software package Topas Academic [24]. For the SXRD data, the Stephens model for anisotropic micro-strain broadening was used for modeling the peak profile parameters [25]. The background of both the SXRD and NPD was modeled using 10 coefficients in the Chebyschev model. For a given space group or combination of space groups, the lattice parameters, atomic positions, isotropic atomic displacement parameters, intensity scale factor, profile shape parameters and background were refined. A-site

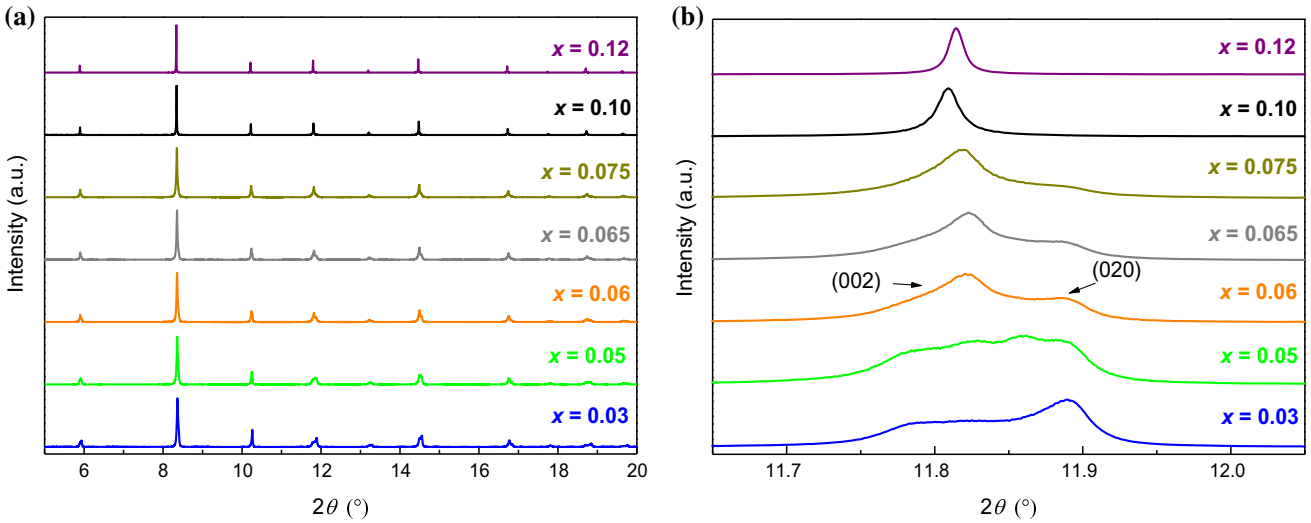

Fig. 1 **a** Room temperature SXRD patterns for $(1-x)$BT–(x)BI ceramics as a function of composition. **b** This shows the modification of (200) reflection upon doping.

atoms (Ba and Bi) were constrained to the origin and equivalent isotropic displacements. The B-site atoms (Ti and In) were also constrained to the same atomic position and isotropic displacements.

Results and discussion

Structural characterization

$(1-x)$BT–(x)BI ceramics were synthesized successfully in the range $0.03 \leq x \leq 0.12$ as determined by XRD. Selected regions of SXRD patterns are shown in Fig. 1a, b. The substitution of BI into BT changes the SXRD data substantially. Thus, the composition $x = 0.03$ has observable peak splitting for multiple reflections similar to the parent BT ($P4mm$). In the case of composition $x = 0.05$, peaks are broad and not well defined. We think this is because it has a core–shell microstructure so the sample is not homogeneous. This issue will be discussed more deeply in the dielectric characterization section. At $x = 0.06$ multiple reflections are still split; however, the relative intensity of them has changed. This is the case of the reflections (002) and (020) as shown in Fig. 1b. For compositions in the range, $0.065 \leq x \leq 0.075$, the reflection (020) decreases the intensity as x increases as shown in Fig. 1b. Finally, at $x \geq 0.10$, a single peak is observed suggesting an increase in symmetry.

Previous structural characterization has been carried out by Datta et al. [15] on the system $(1-x)$BT–(x)BI, where x is 0.03–0.25. Based on Rietveld analysis, they determined that compositions in the range $0.03 \leq x \leq 0.07$ crystallize in $P4mm$ and when $x \geq 0.15$ the structure is cubic with space group $Pm\bar{3}m$. Interestingly, they reported that composition $x = 0.10$ acts as a bridge between the tetragonal and cubic structures, where its structure was determine to be multi-phase with $P4mm$ (~18 wt%) + $R3m$ (~82 wt%) space groups. In our structural study, initially a Rietveld refinement was performed for the composition $x = 0.03$ using the structural parameters previously reported in $P4mm$ by Datta et al. However, a good fit was not achieved giving a goodness of fit parameter R_{wp} of 12.52% (Fig. 2a). Upon careful inspection of the SXRD data, it was observed that reflections are less split compared to the previous published data on this system at $x = 0.03$ and there were clearly peaks in the pattern that were not fit using the single-phase model [15]. Therefore, a multi-phase Rietveld refinement for $x = 0.03$ in $P4mm + R3m$ was attempted using as starting model the structural parameters previously published for $x = 0.10$. In this case, a better fit was achieved with an $R_{wp} = 7.83\%$ where the unindexed peaks from the $P4mm$ model are now fit as Fig. 2b shows. The combination of space groups $P4mm + Pm\bar{3}m$ was also tried for $x = 0.03$. However, the displacement parameters of the B-site for the cubic component, refined to negative values. Datta et al. came to same conclusion for $x = 0.10$, as the isotropic displacement parameters of all atoms for the cubic structure were refined to negative and large numbers [15]. Thus,

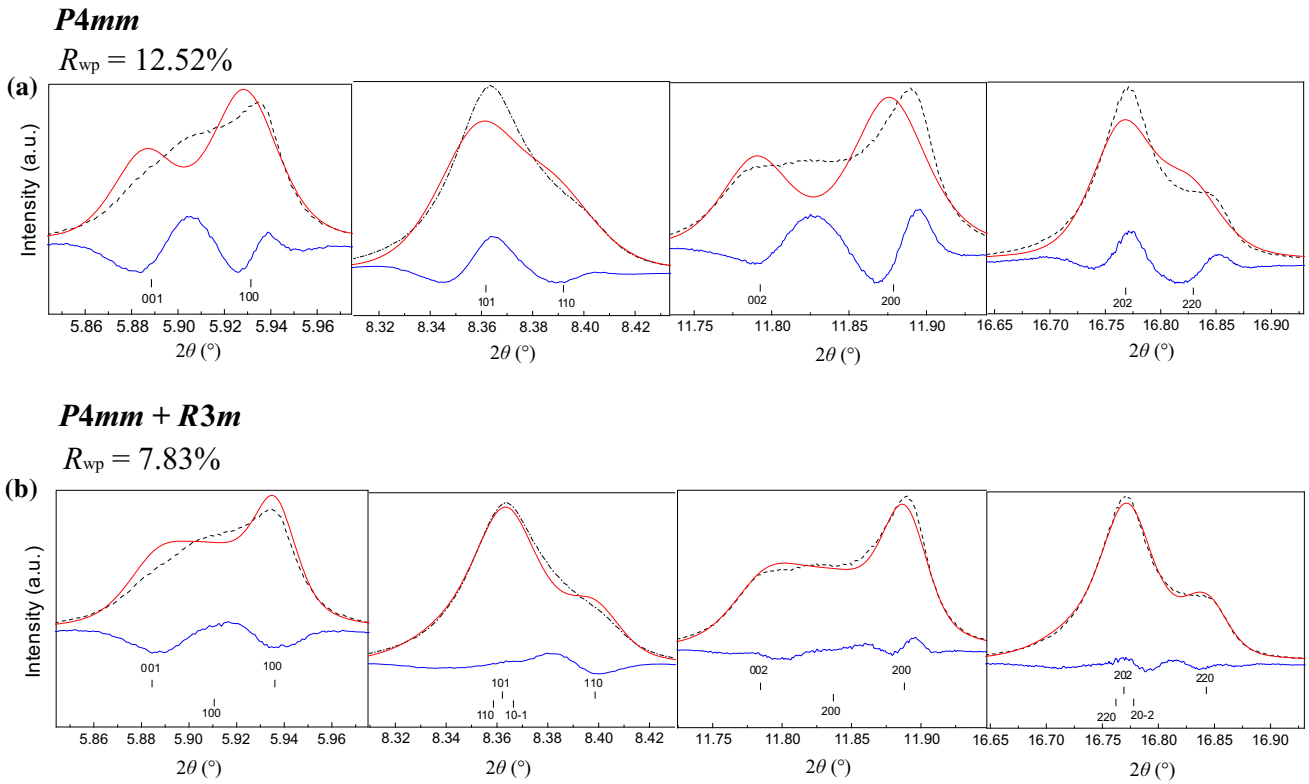

Fig. 2 The fits of selected reflections in Rietveld refinements of $x = 0.03$ using **a** single-phase *P*4*mm* and **b** multi-phase *P*4*mm* and *R*3*m* with the upper *tic marks* from *P*4*mm* and the lower *tic marks* from *R*3*m* for SXRD data. The *black circles* represent the observed data; the *red solid line* represents the model, while the *blue* difference *curve* is below.

replacing the cubic $Pm\bar{3}m$ by a rhombohedral model *R*3*m*, which has more degrees of freedom than $Pm\bar{3}m$ resulted in positive displacement parameters for all atoms. We therefore consider the multi-phase Rietveld refinement for $x = 0.03$ in *P*4*mm* + *R*3*m* to be a reasonable approximation to the structures observed by diffraction. Selected reflections refined using the two different models are shown in Fig. 2. This result clearly demonstrates that a phase combination model in *P*4*mm* + *R*3*m* (Fig. 2b) describes the measured diffraction pattern better than a single-phase refinement (Fig. 2a). For this $x = 0.03$ composition, the phase fraction can be modeled at 50 wt% *P*4*mm* and 50 wt% *R*3*m* with the amount of the *R*3*m* phase increasing up to the $x = 0.075$ composition. This increase in the amount of *R*3*m* phase corresponds with an increase in Bi^{3+} cations on the A-site makes sense in context with the transition to relaxor ferroelectric properties (discussed below) along with the tendency of ambient pressure Bi-based perovskites to displace along $[111]_p$ as in $Bi(Fe_{2/8}Ti_{3/8}Mg_{2/8})O_3$ [26] and $BiFeO_3$ [27]. When $x \geq 0.10$, an increase in symmetry is observed in the SXRD pattern (Fig. 1b). For $x = 0.12$, a refinement in $Pm\bar{3}m$ was attempted as described by Datta et al. for the compositions with high symmetry obtaining an $R_{wp} = 8.45\%$. However, the cubic space group $Pm\bar{3}m$ did not account well for the intensities of some reflections in the SXRD data as Fig. 3a shows. Furthermore, the cubic space group could not model some shoulders in the NPD data, Fig. 3c. A single-phase rhombohedral space group *R*3*m* fit was also attempted and negative values for the isotropic displacement parameters for the B-site were obtained. Therefore, a multi-phase Rietveld refinement in $Pm\bar{3}m$ + *R*3*m* was performed and a satisfactory fit was achieved with an $R_{wp} = 7.58\%$. As Fig. 3b, d shows, this multi-phase refinement better models the intensities and the shoulders in the NPD data. Thus, the structure of compositions in the range $0.10 \leq x \leq 0.12$ was solved as a mixture of $Pm\bar{3}m$ + *R*3*m* with the amount of $Pm\bar{3}m$ increasing with *x* content as expected from ~21wt%. $Pm\bar{3}m$ + ~79 wt% *R*3*m* to ~26 wt% $Pm\bar{3}m$ + ~74 wt% *R*3*m* for $x = 0.10$ and 0.12, respectively. Final refined values of each composition are listed in

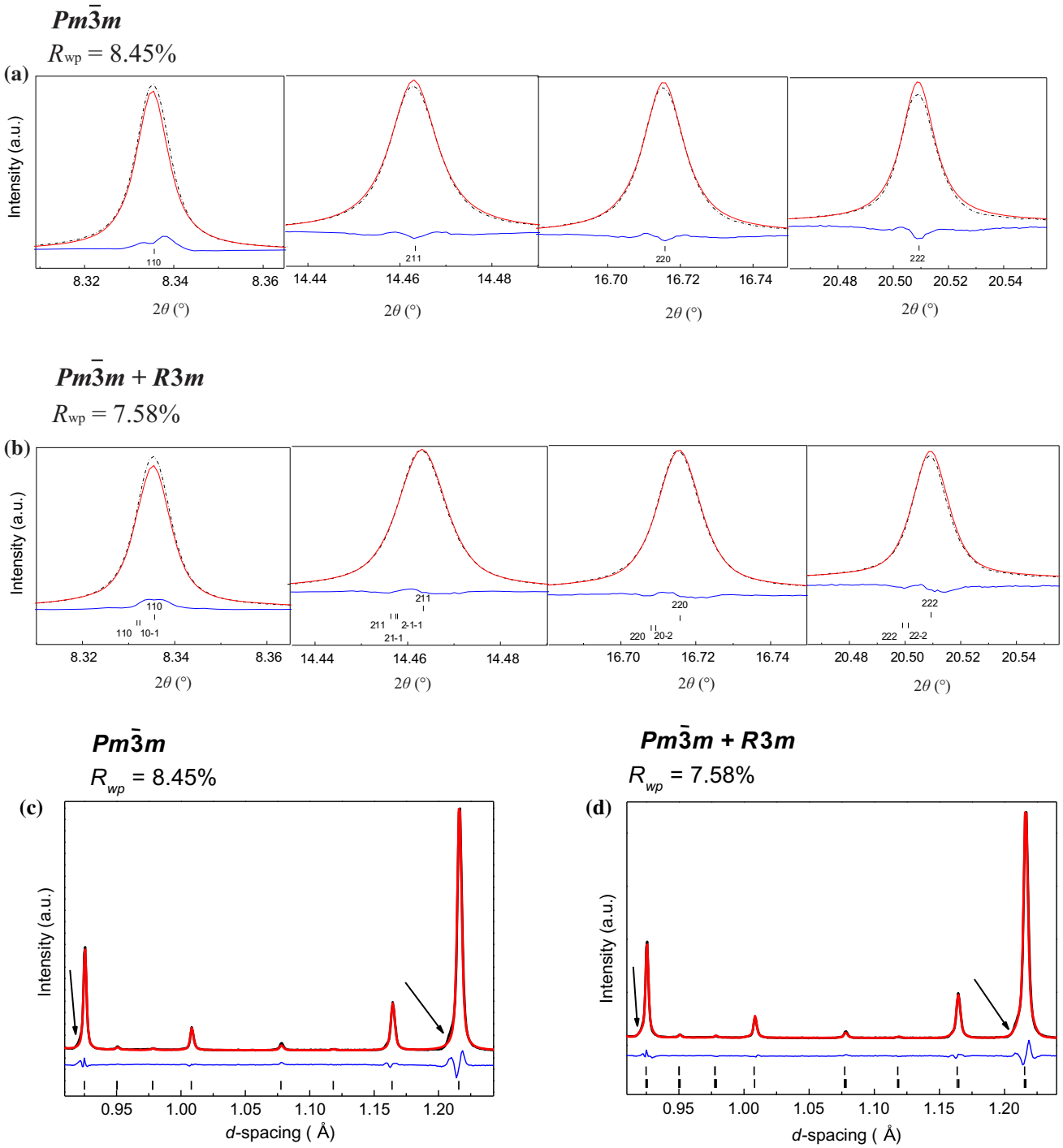

Fig. 3 The fits of selected reflections in Rietveld refinements of $x = 0.12$ using **a**–**c** single-phase $Pm\bar{3}m$ and **b**–**d** multi-phase $Pm\bar{3}m$ and $R3m$ with the upper *tic marks* from $Pm\bar{3}m$ and the lower *tic marks* from $R3m$. The SXRD data is on top and NPD data on the bottom. The *black circles* represent the observed data; the *red solid line* represents the model, while the *blue* difference *curve* is below.

Table 1. Additional refined values (atomic positions and isotropic displacement parameters) are listed in Table S1 (supplementary information).

These structural determinations differ from Datta et al.'s which found the structure to be single-phase $P4mm$ when $x < 0.10$, multi-phase $P4mm + R3m$ at

Table 1 Structural parameters from the combined Rietveld refinement of $(1 - x)$BT–(x)BI ceramics using APS and POWGEN data

Composition (x)	Space group	Phase (wt%)	Lattice parameters (Å) and angles (°)	Quality of fit
0.03	$P4mm$	50	$a = 4.0009$ (6) $c = 4.0346$ (9)	$R_{wp} = 7.83\%$
	$R3m$	50	$a = 4.019$ (1) $\alpha = 89.84$ (4)	
0.05	$P4mm$	38	$a = 4.0039$ (4) $c = 4.035$ (1)	$R_{wp} = 8.91\%$
	$R3m$	62	$a = 4.021$ (1) $\alpha = 89.89$ (5)	
0.06	$P4mm$	28	$a = 4.0023$ (9) $c = 4.036$ (1)	$R_{wp} = 7.53\%$
	$R3m$	72	$a = 4.0226$ (4) $\alpha = 89.957$(6)	
0.065	$P4mm$	20	$a = 4.002$ (1) $c = 4.039$ (2)	$R_{wp} = 7.72\%$
	$R3m$	80	$a = 4.0230$ (3) $\alpha = 89.99$ (9)	
0.075	$P4mm$	14	$a = 4.0019$ (5) $c = 4.041$ (2)	$R_{wp} = 8.11\%$
	$R3m$	86	$a = 4.0243$ (2) $\alpha = 89.97$ (4)	
0.10	$Pm\bar{3}m$	21	$a = 4.037$ (2)	$R_{wp} = 10.31\%$
	$R3m$	79	$a = 4.02722$ (9) $\alpha = 89.99$ (5)	
0.12	$Pm\bar{3}m$	26	$a = 4.031$ (1)	$R_{wp} = 7.58\%$
	$R3m$	74	$a = 4.03189$ (4) $\alpha = 89.952$ (9)	

$x = 0.10$ and single-phase $Pm\bar{3}m$ when $x > 0.10$. The synthesis in the Datta paper reported pellets were sintered for structural analysis at 1400 °C for 4 h, with no mention of a sacrificial powder being used. Our attempts to replicate this synthesis resulted in the inability to achieve reproducible physical properties on different pellets of the same composition from the same batch. Attempts were made to lower the sintering temperature to 1300 °C for 1–2 h buried in sacrificial powder, which also resulted in the inability to reproduce physical property measurements. This inconsistency in properties measurements indicates that the higher sintering temperatures likely lead to volatility of the bismuth cations. Therefore, we had to decrease the sintering temperature to 1200 °C which had an impact on the structure of the entire series of compositions. Although obtaining accurate compositional analysis of Bi-based compounds is notoriously difficult, ICP measurements were performed on the $x = 0.03$ composition to determine whether this theory could be accurate. The expected Ba/Bi molar ratio is 0.97:0.03. The ratio determined by ICP measurements using the compound sintered according to the Datta paper was 0.97:0.026, while the compound sintered at lower temperatures was 0.97:0.029. While the difference is small, it does show Bi^{3+} volatilization could be occurring when sintering at the higher temperatures reported by Datta.

Dielectric characterization

Relative permittivity for $(1 - x)$BT–(x)BI ceramics across the full range of compositions, $0.03 \leq x \leq 0.12$, as a function of temperature are shown in Fig. 4a. None of the compositions exhibit a sharp phase transition typical of a ferroelectric material like in the parent compound BT. In this system, the peaks become broader with content of x (Fig. 4a, d), where a broad frequency dependent maximum permittivity is

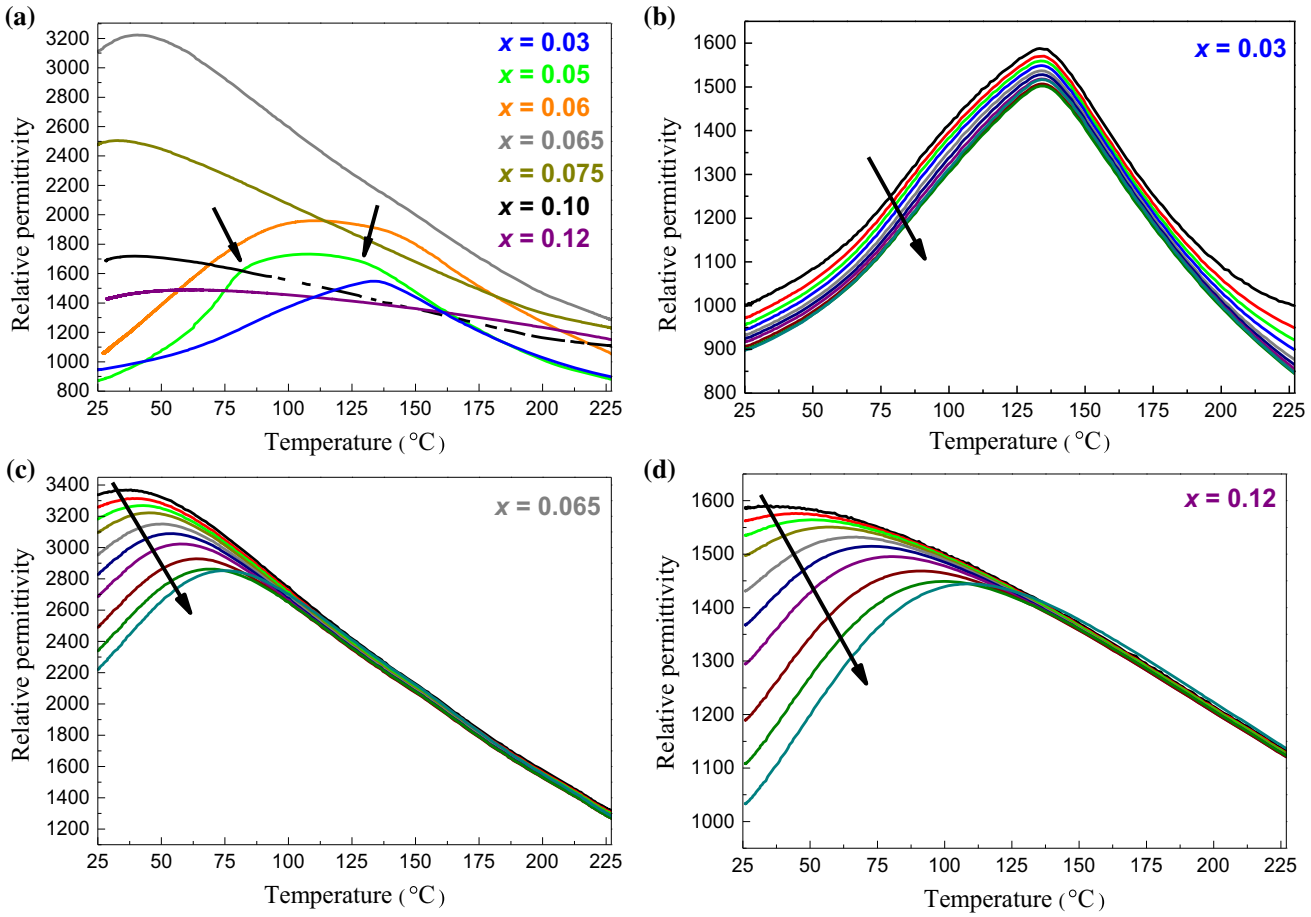

Fig. 4 Temperature dependence of relative permittivity of: **a** $(1 - x)$BT–(x)BI ceramics measured at 10 kHz. **b** $x = 0.03$. **c** $x = 0.065$ and **d** $x = 0.12$ at different frequencies from 1 kHZ to 1 MHz.

observed, indicating a transition to a weakly coupled relaxor material [28, 29]. This behavior has been observed for other related systems such as: $BaTiO_3$–$BiScO_3$ (BT–BS) [28], $BaTiO_3$–$Bi(Zn_{0.5}Ti_{0.5})O_3$ (BT–BZT) [30, 31], and $BaTiO_3$–$BiAlO_3$ (BT–BA) [32]. In this BT–BI system, the temperature of maximum permittivity (T_{max}) decreases as more BI is added into the solid solution. It might be assumed that the T_{max} should have increased in relation to BT because the T_c for BT is ~120 °C [17], while the T_c of BI is >600 °C [18]. However, this trend of a ferroelectric-relaxor ferroelectric transition with T_{max} decreasing has also been observed in the similar system BT–BA [32]. The reason for the trends in T_{max} is unclear in the literature, and further investigations are necessary to understand the nature of the change as a function of composition. In contrast to these BT-based materials, solid solutions of $PbTiO_3$ with $BiAlO_3$ (PT–BA) [33], $BiInO_3$ (PT–BI) [20], and $BiScO_3$ (PT–BS) [19, 34, 35] maintain ferroelectricity over much larger composition ranges sometimes through a phase transition where the PT–BS materials have an MPB.

For the $x = 0.05$ composition, two permittivity peaks are observed as indicated by black arrows in Fig. 4a at about 90 and 125 °C. This effect could be from a local core–shell microstructures resulting from a difficulty to homogenize during sintering and is commonly found at low substitution percentages in these types of systems. This phenomenon has been observed in the system $(1 - x)$BT–xBS by Ogihara et al. [28] and 0.98BT–0.02BA by Zheng et al. [32]. In BT–BS when $x = 0.05$, two clear permittivity peaks appear for ceramics sintered for 1 h. Based on TEM and elemental analysis, they claim that the cores of the grains are rich in BT and responsible for the higher temperature peak. In contrast, the shell is rich in BS and accounts for the lower temperature peak.

Room temperature dielectric measurements of both relative permittivity and loss show frequency dispersion (Fig. 5a, b respectively). The data show that

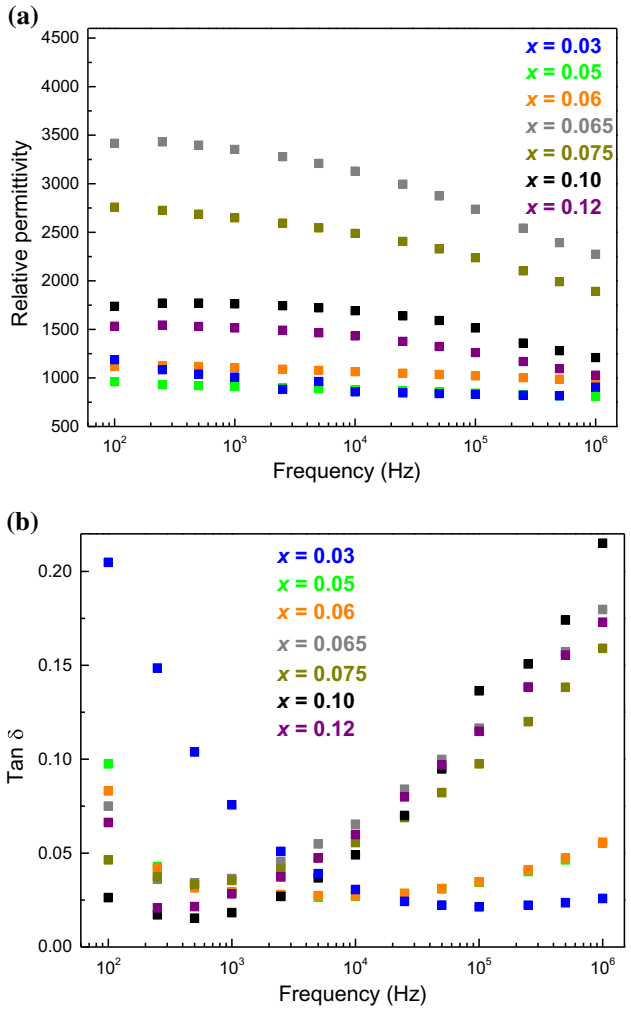

Fig. 5 **a** Dielectric constant and **b** loss tangent as a function of frequency at room temperature for $(1-x)$BT–(x)BI ceramics.

the permittivity is the highest for $x = 0.065$ at the whole frequency range (Fig. 5a). The maximum relative permittivity value at 10 kHz for $x = 0.065$ is 3220, which is much lower than that of ferroelectric BT (25000) [32] but similar to the permittivity found upon the addition of BA in 0.95BT–0.05BA (3500) which also becomes relaxor-like [32]. The loss also shows frequency dispersion where a dielectric relaxation is present that shifts as a function of frequency (Fig. 5b). The $x = 0.03$ sample has the highest loss at low frequencies (0.2048 at 100 Hz), but the lowest loss at higher frequencies (0.0258 at 1 MHz) where the $x = 0.10$ and $x = 0.12$ compositions have the lowest loss at low frequencies (0.0263 and 0.0663, respectively, at 100 Hz) and high loss at higher frequencies (0.215 and 0.1729, respectively, at 1 MHz). The frequency dispersion is also evident by examining ΔT_{max} (the difference between T_{max} measured at 250 and 10 kHz), which was determined from the dielectric curves for all the compositions. It is observed that ΔT_{max} generally increases with the content of x, which is another indication that BT–BI ceramics transition to a relaxor state as x increases. Data for T_{max}, relative permittivity and tan δ for compositions $0.03 \leq x \leq 0.12$ are listed in Table 2.

Ferroelectric hysteresis

Ferroelectric P–E hysteresis loop measurements were taken at room temperature under an applied electric field of 40 kV/cm at 0.1 Hz for all compositions as shown in Fig. 6 and Fig. S11. At $x = 0.03$, the polarization loop resembles that of the ferroelectric parent compound BT. This composition shows a nearly saturated loop with a remnant polarization (P_r) of 3.25 μC/cm^2. As the amount of BI increases to $x = 0.075$, P_r decreases while still showing hysteresis, indicating the presence of nano-sized polar domains and a transition to a relaxor ferroelectric. This agrees

Table 2 Dielectric permittivity data for $(1-x)$BT–(x)BI ceramics

Composition (x)	T_{max} (°C)	Relative permittivity at T_{max}	Room temperature		ΔT_{max} (°C)
			Relative permittivity	tanδ	
0.03	133	1549	950	0.031	~0.5
0.05	118	1730	870	0.028	2
0.06	110	1960	1056	0.027	5
0.065	45	3220	3100	0.07	13
0.075	37	2500	2480	0.06	21
0.1	47	1720	1687	0.05	25
0.12	62	1489	1430	0.062	30

Data obtained from 10 kHz measurement. ΔT_{max} is the difference between T_{max} measured at 250 and 10 kHz

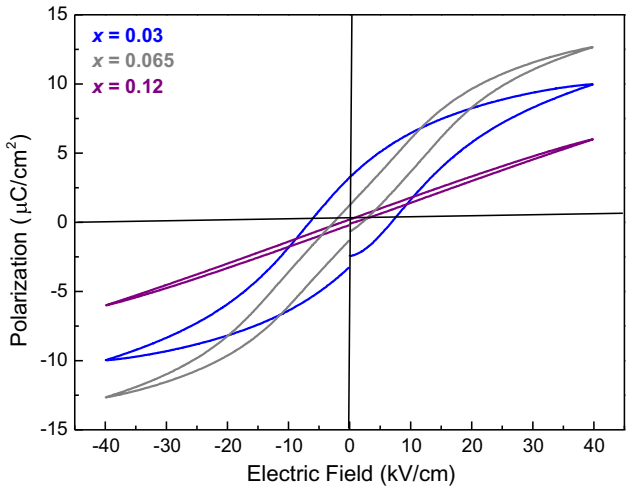

Fig. 6 Room temperature *P–E* hysteresis loops measured at 0.1 Hz for $(1-x)$BT–(x)BI ceramics for $x = 0.03$ (*blue*), $x = 0.065$ (*gray*) and $x = 0.12$ (*purple*).

well with the dielectric permittivity data. For compositions $x = 0.10, 0.12$, the *P–E* loops are nearly linear, showing hysteresis, but no saturation of dipoles. While these compositions still show relaxor behavior, this could be due to the size of the nanodomains or presence of increasing non-polar cubic $Pm\bar{3}m$ phase as determined by the Rietveld refinements.

The maximum polarization (P_{max}) is achieved for composition $x = 0.065$ with a value of 12.6 μC/cm^2 and is referred to as the critical composition. This data is also consistent with the dielectric results obtained where the maximum value for the relative permittivity is also at $x = 0.065$. This enhancement of dielectric and ferroelectric properties at the critical composition can be attributed to a phase transformation from a ferroelectric to a relaxor phase. This phenomenon has been previously observed in other systems such as: $(Bi_{0.5}Na_{0.41}K_{0.09})_{1-x}La_xTiO_3$ where the value of P_{max} is about 40 μC/cm^2 at the critical composition $x = 0.03$ [36] and for $(0.94–x)(Na_{0.5}Bi_{0.5})TiO_3$-$0.06BaTiO_3$–$xBi(Me_{0.5}Ti_{0.5})O_3$ (Me = Zn (Z), Ni (N), Mg(M), Co(C)) (NBT–BT–B$(Me_{0.5}Ti_{0.5})O_3$ with P_{max} values ranging between 35 and 40 μC/cm^2 at the critical compositions for 0.0275BZT, 0.03BMT, 0.035BNiT and 0.04BCT [37, 38]. The P_{max} values of other related systems are 14 μC/cm^2 for the relaxor 0.95BT–0.05BA [32] and 40 μC/cm^2 for the ferroelectric 0.64PT–0.36BS [35]. Values for P_{max} and P_r are listed in Table 3.

Piezoelectric properties

The electromechanical strain was investigated at room temperature with a measurement frequency of 0.1 Hz and an applied electric field of 40 kV/cm. Figure 7a shows the bipolar strain-electric field loops for compositions $x = 0.03, 0.065$ and 0.12. For the compositions in the range $0.03 \leq x \leq 0.075$, the bipolar strain exhibits the classic butterfly loop which indicates bulk piezoelectricity. These compositions also show evidence of ferroelectric switching in their negative strain component. However, for $x \geq 0.10$, the butterfly loops disappear and transform to parabolic curves with negligible hysteresis and no negative strain component as shown in Fig. 7a and Fig. S12a. The decrease and eventual elimination of the negative strain component as x increases indicates an increase in the ergodic behavior of the relaxor ferroelectric [39]. When the transition occurs from ferroelectric to relaxor ferroelectric, the continued presence of negative strain indicates that some of the polar nanoregions are frozen and the application of an external field during the *S–E* measurement causes ferroelectric switching. Eventually, at $x = 0.10$, the negative strain component disappears due to the fluctuation of dipoles and no switching

Table 3 Maximum polarization (P_{max}) and remnant polarization (P_r) from *P–E* measurements

Composition (x)	P_{max} (μC/cm^2)	P_r (μC/cm^2)	Strain (%)	d^*_{33} (pm/V)	h (%)
0.03	9.96	3.25	0.048	120	17
0.05	9.23	2.4	0.046	115	17
0.06	9.75	3.06	0.059	147	26
0.065	12.64	1.21	0.104	260	11
0.075	11.13	0.55	0.06	150	11
0.1	7.65	0.4	0.031	78	11
0.12	5.98	0.19	0.010	25	0

Strain from unipolar *S–E* field loops, effective piezoelectric coefficient d^*_{33}(=S_{max}/E_{max}, where S_{max} is the strain observed at the maximum field E_{max}) and finite hysteresis h (=$\Delta S/S_{max}$; where ΔS is the width of the widest part of the loop)

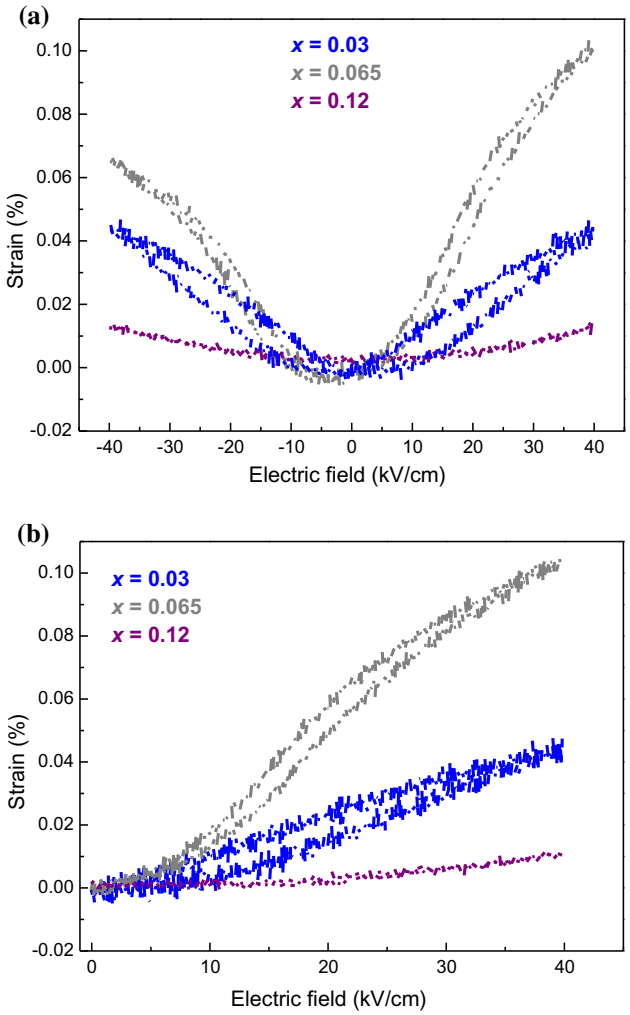

Fig. 7 For $(1-x)$BT–(x)BI ceramics room temperature: **a** bipolar and **b** monopolar strain-electric field measurements performed at 0.1 Hz for $x = 0.03$ (*blue*), $x = 0.065$ (*gray*) and $x = 0.12$ (*purple*).

occurs. The results of the *S*–*E* measurements are in good agreement with both the *P*–*E* loops and permittivity measurements. The strain response of the studied material under unipolar *E* cycling was measured to investigate its potential for actuators applications, Fig. 7b and Fig. S12b. The highest strain value achieved is by the critical composition $x = 0.065$ with a value of 0.104%, which is higher than that of 0.95BT–0.05BA (0.07%) [32] but lower than 0.64PT–0.36BS (0.17%) [35], $(Bi_{0.5}Na_{0.41}K_{0.09})_{0.97}La_{0.03}TiO_3$ (0.35%) [36] and the critical compositions specified before for the NBT-BT-$B(Me_{0.5}Ti_{0.5})O_3$ system (0.35–0.40%) [37, 38]. This result is consistent with the dielectric and *P*–*E* loops measurements where the highest values of the relative permittivity and P_{max} also come from $x = 0.065$ as Fig. 8 and Table 3 show. All the unipolar loops exhibit nonlinearity with finite hysteresis (*h*) values (Table 3). The composition $x = 0.065$ in particular exhibits a high nonlinear-strain-electric field behavior. The nonlinearity could be due to extrinsic effects (as opposed to intrinsic effects or lattice response) that arise mainly from domain wall motion, although additional contributions can occur, such as grain boundary effects and displacement of inter-phase boundaries [2, 40, 41]. As Fig. 8a shows, for the $P4mm + R3m$ region, $0.03 \leq x \leq 0.75$, d^*_{33} increases sharply for the critical composition $x = 0.065$ with a value of 260 pm/V. However, as expected for the $Pm\bar{3}m + R3m$ region, $x \geq 0.10$, d^*_{33} decreases with x being 25 pm/V for $x = 0.12$. This agrees well with the linear *P*–*E* loops and P_r decreasing to nearly zero in this region. For comparison, for the NBT-BT-$B(Me_{0.5}Ti_{0.5})O_3$ system d^*_{33} values at the critical compositions range between 550 and 600 pm/V. Moreover, for the critical composition $x = 0.065$, a significant reduction in the P_r can be clearly observed (Fig. 8b), resulting in a relaxor-like *P*–*E* loop (Fig. 6) possibly due to the coexistence of ferroelectric and relaxor phases [36, 38]. This behavior has been observed in the similar systems NBT-BT-$B(Me_{0.5}Ti_{0.5})O_3$ and $(Bi_{0.5}Na_{0.41}K_{0.09})_{1-x}La_xTiO_3$ where the P_r is decreased and d^*_{33} enhanced for the critical compositions. Piezoresponse force microscopy studies have shown that for $(Bi_{0.5}Na_{0.41}K_{0.09})_{0.97}La_{0.03}TiO_3$ the giant strain response ($d^*_{33} = 857$ pm/V) was accompanied by the nanoscale coexistence of ferroelectric and relaxor phases [36]. Values for strain, d^*_{33} and *h* for $(1-x)$BT–(x)BI ceramics are collected in Table 3.

In this study, on the basis of the structural analysis, dielectric, ferroelectric and piezoelectric properties discussed above, a phase diagram for the system $(1-x)$BT–(x)BI was established as Fig. 9 shows. In addition, above each composition range the corresponding structures are displayed. We can observe that T_{max} decreases with BI content linearly in the range $0.03 \leq x \leq 0.06$. However, at the critical composition $x = 0.065$, where the large strain response is observed, T_{max} decreases sharply increasing slightly again when $x \geq 0.10$ at the multi-phase region $Pm\bar{3}m + R3m$. Therefore, from the measured electrical properties, we concluded that the large strain response at $x = 0.065$ is closely associated with the composition and temperature-induced phase transformation leading to the coexistence of ferroelectric and relaxor phases.

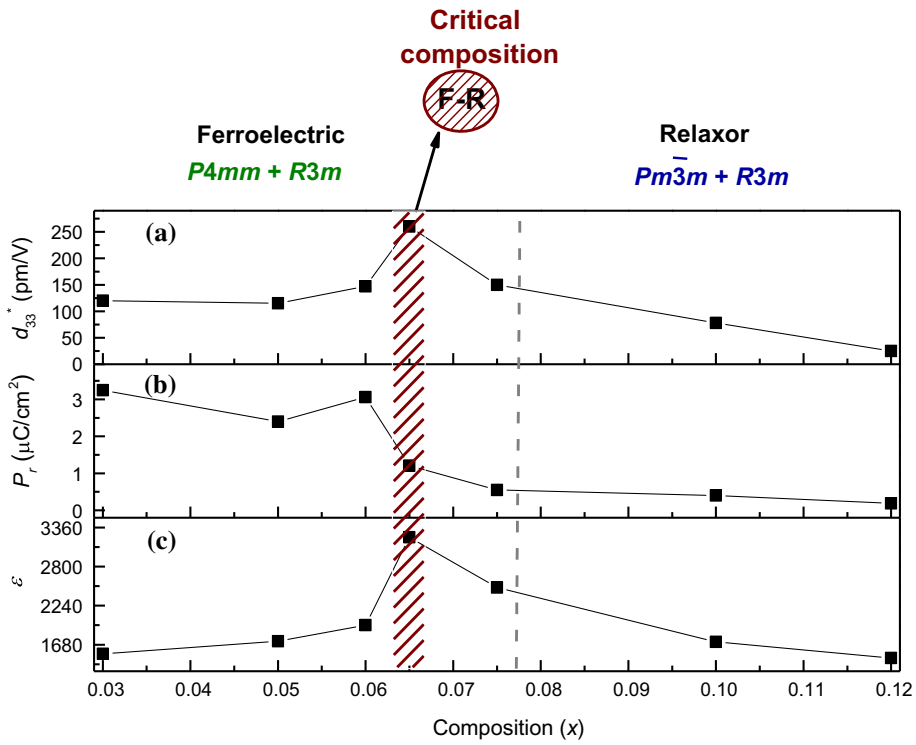

Fig. 8 *a* Variation of the effective piezoelectric coefficient (d_{33}^*) calculated from monopolar *S–E* loops. *b* Remnant polarization (P_r) and *c* relative permittivity (ε) with BI content (x). The *gray dashed line* indicates approximate the region where a change in symmetry takes place from $P4mm + R3m$ to $Pm\bar{3}m + R3m$, while the *dark red* shadow area indicates the critical composition $x = 0.065$.

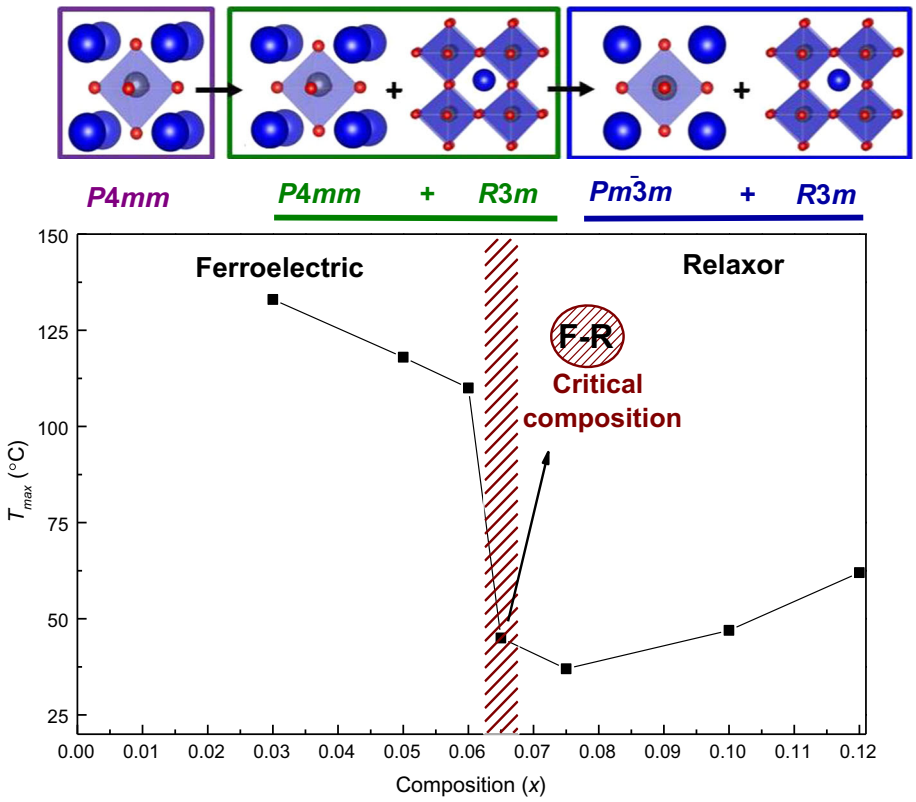

Fig. 9 Schematic phase diagram for the $(1 - x)$BT–(x)BI ceramics. The T_{max} values are those from Table 2 and were taken from the 10 kHz permittivity data.

Morphotropic phase boundary and polarization extension

While an enhanced piezoelectric response is evident at $x = 0.065$, we do not consider this system to have an MPB but a critical composition with a mixture of ferroelectric and relaxor phases as in the systems NBT-BT-$B(Me_{0.5}Ti_{0.5})O_3$ and $(Bi_{0.5}Na_{0.41}K_{0.09})_{1-x}La_xTiO_3$ [36–38]. As the amount of BI is added to the system, the material transitions from a traditional ferroelectric material as the parent BT to a relaxor ferroelectric. The structural transition is not a sharp sudden transition, rather the percent of the pseudo-cubic rhombohedral phase slowly increases in the range $0.03 \leq x \leq 0.075$ and the frequency dependence of T_{max} in the permittivity measurements becomes broader as a function of x. This is similar to the systems BT–BA [32] and BT–BS [28]. Alternatively, when these same phases are used in solid solutions with PT as in PT–BI [20] PT–BS [19, 34, 35] and PT–BA [33], the ferroelectric phases remains over a large composition range and in PT–BS [19, 34, 35], an MPB between two ferroelectric phases forms. Solid solutions of Bi-based perovskites with BT likely lead to relaxor ferroelectrics due to the formation of polar nanodomains resulting from competition on the A-site where Ba^{2+} prefers a more symmetric coordination environment and Bi^{3+} prefers a distorted coordination environment due to the lone pair effect. Alternatively when Bi-based compounds are used with PT, the tetragonality is reduced, but the system maintains its ferroelectric properties as the structure changes because both cations cause distortions from the presence of a lone pair, eliminating the instability caused by the different A-site cations.

As this system is not considered to have a morphotropic phase boundary, it does not have a polarization extension mechanism as predicted [8, 10]. As mentioned above, compositions where $x \geq 0.10$ are multi-phase and contain the cubic $Pm\bar{3}m$ and rhombohedral $R3m$ structures, not single phase cubic as reported by Datta. While this particular material does not meet the criteria for a material with a polarization extension, we believe that it is important to continue the search for these nontraditional piezoelectrics.

Conclusions

With the introduction of BI into BT, a gradual phase transition from a polar tetragonal structure to a multi-phase tetragonal and rhombohedral structure to a multi-phase pseudo-cubic structure was observed. As the content of BI increases, a ferroelectric to relaxor ferroelectric transition occurs as the frequency dependence broadens and T_{max} decreases. The relative permittivity, maximum polarization and effective piezoelectric coefficient are maximized for the critical composition $x = 0.065$ as a result of the coexistence of ferroelectric and relaxor phases with a strain value of $\sim 0.104\%$ and a d^*_{33} of 260 pm/V under a moderate electric field of 40 kV/cm.

Acknowledgements

This material is based upon work supported by the National Science Foundation under Grant No. DMR-1606909. Use of the Advanced Photon Source at Argonne National Laboratory was supported by the U. S. Department of Energy, Office of Science, Office of Basic Energy Sciences, under Contract No. DE-AC02-06CH11357. This research used resources at the Spallation Neutron Source, a DOE Office of Science User Facility operated by the Oak Ridge National Laboratory. We would like to thank Saul Lapidus and Lynn Ribaud of 11-BM at the APS and Ashfia Huq, Pam Whitfield, and Melanie Kirkham of POWGEN at the SNS for their assistance with our mail-in samples. We would also like to thank David Cann at Oregon State University for use of his equipment for the permittivity measurements and helpful discussions.

Compliance with ethical standards

Conflicts of interest The authors declare that they have no conflicts of interest regarding this work.

Electronic supplementary material: The online version of this article (doi:10.1007/s10853-017-0770-x) contains supplementary material, which is available to authorized users.

References

[1] Panda KP (2009) Review: environmental friendly lead-free piezoelectric materials. J Mater Sci 44(19):5049–5062. doi:10.1007/s10853-009-3643-0

[2] Roedel J, Jo W, Seifert KTP, Anton EM, Granzow T, Damjanovic D (2009) Perspective on the development of lead-free piezoceramics. J Am Ceram Soc 92(6):1153–1177

[3] Damjanovic D, Klein N, Li J, Porokhonskyy V (2010) What can be expected from Lead-free piezoelectric materials? Funct Mater Lett 3(1):5–13

[4] Gensch CO, Baron Y, Blepp M, Moch K, Moritz S, Deubzer O (2016) Study to assess renewal requests for 29 RoHS 2 Annex III exemptions

[5] Fu HX, Cohen RE (2000) Polarization rotation mechanism for ultrahigh electromechanical response in single-crystal piezoelectrics. Nature 403(6767):281–283

[6] Guo R, Cross LE, Park SE, Noheda B, Cox DE, Shirane G (2000) Origin of the high piezoelectric response in $PbZr_{1-x}Ti_xO_3$. Phys Rev Lett 84(23):5423–5426

[7] Bell AJ (2006) Factors influencing the piezoelectric behaviour of PZT and other "morphotropic phase boundary" ferroelectrics. J Mater Sci 41(1):13–25. doi:10.1007/s10853-005-5913-9

[8] Damjanovic D (2009) Comments on origins of enhanced piezoelectric properties in ferroelectrics. IEEE Transact Ultrason Ferroelectr Freq Control 56(8):1574–1585

[9] Damjanovic D (2005) Contributions to the piezoelectric effect in ferroelectric single crystals and ceramics. J Am Ceram Soc 88(10):2663–2676

[10] Damjanovic D (2010) A morphotropic phase boundary system based on polarization rotation and polarization extension. Appl Phys Lett 97(6):062906-3

[11] Yao Y, Zhou C, Lv D, Wang D, Wu H, Yang Y, Ren X (2012) Large piezoelectricity and dielectric permittivity in $BaTiO_3$-x$BaSnO_3$ system: the role of phase coexisting. EPL 98(2):27008-6

[12] Akiyama M, Kamohara T, Kano K, Teshigahara A, Takeuchi Y, Kawahara N (2009) Enhancement of piezoelectric response in scandium aluminum nitride alloy thin films prepared by dual reactive cosputtering. Adv Mater 21(5):593–596

[13] Tasnadi F, Alling B, Hoglund C, Wingqvist G, Birch J, Hultman L, Abrikosov IA (2010) Origin of the anomalous piezoelectric response in wurtzite $Sc_xAl_{1-x}N$ alloys. Phys Rev Lett 104(13):137601–137604

[14] Von AA, Bantle W (1944) Der inverse Piezoeffekt des seignetteelektrischen kristalls KH_2PO_4. Helv Phys Acta 17:298–318

[15] Datta K, Suard E, Thomas PA (2010) Compositionally driven ferroelectric phase transition in x$BiInO_3$-(1 − x) $BaTiO_3$: a lead-free perovskite-based piezoelectric material. Appl Phys Lett 96(22):221902–221903

[16] Megaw HD (ed) (1957) Ferroelectricity in crystals. Methuen, London

[17] Jaffe H (1958) Piezoelectric ceramics. J Am Ceram Soc 41(11):494–498

[18] Belik AA, Stephanovich SY, Lazoryak BI, Takayama-Muromachi E (2006) $BiInO_3$: a polar oxide with $GdFeO_3$-type perovskite structure. Chem Mat 18(7):1964–1968

[19] Eitel RE, Randall CA, Shrout TR, Rehrig PW, Hackenberger W, Park SE (2001) New high temperature morphotropic phase boundary piezoelectrics based on $Bi(Me)O_3$-$PbTiO_3$ ceramics. Jpn J Appl Phys 40(10):5999–6002

[20] Duan RR, Speyer RF, Alberta E, Shrout TR (2004) High curie temperature perovskite $BiInO_3$-$PbTiO_3$ ceramics. J Mater Res 19(7):2185–2193

[21] Li CL, Wang H, Wang B, Wang R (2007) First-principles study of the structure, electronic, and optical properties of orthorhombic $BiInO_3$. Appl Phys Lett 91(7):071902–071903

[22] Li CL, Wang ZQ, Ma DC, Wang CY, Wang BL (2014) Phase stability, electronic structure and optical properties of $BiInO_3$ under strain. Jpn J Appl Phys 47(5):055302–055307

[23] Wang J, Tony BH, Lee PL, Ribaud L, Antao SM, Kurtz C, Ramanathan M, Von Dreele RB, Beno MA (2008) A dedicated powder diffraction beamline at the advanced photon source: commissioning and early operational results. Rev Sci Instrum 79(8):085105–085107

[24] Coelho AA (2000) Whole-profile structure solution from powder diffraction data using simulated annealing. J Appl Crystallogr 33(2):899–908

[25] Stephens PW (1999) Phenomenological model of anisotropic peak broadening in powder diffraction. J Appl Crystallogr 32:281–289

[26] Bridges CA, Allix M, Suchomel MR, Kuang X, Sterianou I, Sinclair DC, Rosseinsky MJ (2007) A pure bismuth a site polar perovskite synthesized at ambient pressure. Angew Chem Int Ed 46:8785–8789

[27] Filip'ev VS, Smol'yaninov IP, Fesenko EG, Belyaev I (1960) Synthesis of $BiFeO_3$ and determination of the unit cell. Kristallografiya 5:958

[28] Ogihara H, Randall CA, Trolier-McKinstry S (2009) Weakly Coupled Relaxor Behavior of $BaTiO_3$–$BiScO_3$. Ceram J Am Ceram Soc 92(1):110–118

[29] Raengthon N, Cann DP (2012) High temperature electronic properties of $BaTiO_3$–$Bi(Zn_{1/2}Ti_{1/2})O_3$–$BiInO_3$ for capacitor applications. J Electroceram 28(2–3):165–171

[30] Huang C, Cann DP (2008) Phase transitions and dielectric properties in $Bi(Zn_{1/2}Ti_{1/2})O_3$–$BaTiO_3$ perovskite solid solutions. J Appl Phys 104(2):024117-4

[31] Bootchanont A, Triamnak N, Rujirawat S, Yimnirun R, Cann DP, Guo RY, Bhalla A (2014) Local structure and evolution of relaxor behavior in $BaTiO_3$–$Bi(Zn_{0.5}Ti_{0.5})O_3$ ceramics. Ceram Int 40(9):14555–14562

[32] Zheng SY, Odendo E, Liu LJ, Shi DP, Huang YM, Fan LL, Chen J, Fang L, Elouadi B (2013) Electrostrictive and

relaxor ferroelectric behavior in $BiAlO_3$-modified $BaTiO_3$ lead-free ceramics. J Appl Phys 113(9):094102–094105

[33] Yu HC, Ren W, Ye ZG (2010) Structural, Dielectric, and Ferroelectric Properties of the $(1 - x)PbTiO_3$-$xBiAlO_3$ Solid Solution. IEEE Transact Ultrason Ferroelectr Freq Control 57(10):2177–2181

[34] Inaguma Y, Miyaguchi A, Yoshida M, Katsumata T, Shimojo Y, Wang RP, Sekiya T (2004) High-pressure synthesis and ferroelectric properties in perovskite-type $BiScO_3$–$PbTiO_3$ solid solution. J Appl Phys 95(1):231–235

[35] Eitel RE, Randall CA, Shrout TR, Park SE (2002) Preparation and characterization of high temperature perovskite ferroelectrics in the solid-solution $(1 - x)BiScO_3$-$xPbTiO_3$. Jpn J Appl Phys 41(4A):2099–2104

[36] Dinh TH, Kang JK, Lee JS, Khansur NH, Daniels J, Lee HY, Yao FZ, Wang K, Li JF, Han HS, Jo W (2016) Nanoscale ferroelectric/relaxor composites: origin of large strain in lead-free Bi-based incipient piezoelectric ceramics. J Eur Ceram Soc 36(14):3401–3407

[37] Bai WF, Chen DQ, Zheng P, Shen B, Zhai JW, Ji ZG (2016) Composition- and temperature-driven phase transition characteristics and associated electromechanical properties in $Bi_{0.5}Na_{0.5}TiO_3$-based lead-free ceramics. Dalton Trans 45(20):8573–8586

[38] Bai WF, Shen B, Zhai JW, Liu F, Li P, Liu BH, Zhang Y (2016) Phase evolution and correlation between tolerance factor and electromechanical properties in BNT-based ternary perovskite compounds with calculated end-member $Bi(Me_{0.5}Ti_{0.5})O_3$ (Me = Zn, Mg, Ni, Co). Dalton Trans 45(36):14141–14153

[39] Jo W, Dittmer R, Acosta M, Zang J, Groh C, Sapper E, Wang K, Roedel J (2012) Giant electric-field-induced strains in lead-free ceramics for actuator applications—status and perspective. J Electroceram 29(1):71–93

[40] Carl K, Hardtl KH (1978) Electrical after-effects in Pb(Ti, Zr)O3 ceramics. Ferroelectrics 17(3–4):473–486

[41] Shrout TR, Zhang SJ (2007) Lead-free piezoelectric ceramics: alternatives for PZT? J Electroceram 19(1):113–126